Research Article | Vol. 30, No. 17 / 15 Aug 2022 / Optics Express 30507
Optics EXPRESS

Interferometric measurements of nonlinear refractive index in the infrared spectral range

GAUDENIS JANSONAS,[1,*] RIMANTAS BUDRIŪNAS,[1,2] MIKAS VENGRIS,[1] AND ARŪNAS VARANAVIČIUS[1]

[1] Vilnius University, Laser Research Center, Saulėtekio Ave. 10, LT- 10222 Vilnius, Lithuania
[2] Light Conversion Ltd., 2b Keramikų str., LT- 10223 Vilnius, Lithuania
[*] gaudenisjansonas@yahoo.com

Abstract: This study presents the development and application of interferometric technique for the measurement of nonlinear refractive index of optical materials, while directly accounting for experimentally determined laser pulse shape and beam profile. The method was employed in a systematic study of nonlinear refractive index on a series of common optical materials used in near and mid-IR spectral range, where experimental data on nonlinear material properties is still scarce. The values of nonlinear refractive index were determined at 1.03 μm, 2.2 μm, and 3.2 μm. The measurement results are compared to the values determined by previous studies (where available), and the influence of cascaded second-order nonlinearities is discussed.

1. Introduction

With rapid advancement in the development of intense ultrashort pulse sources operating at wavelengths above 2 μm, there has been much interest in nonlinear optical response of materials in this spectral region. In most cases, these sources are based on nonlinear frequency converters containing multiple optical components [1–7] where the intensities of propagating light pulses are high enough to significantly deteriorate pulse and beam quality due to beam self-focusing, spatial beam distortion and break up, self-phase modulation (SPM), etc. [8]. Accurate estimates of the nonlinear refractive index n_2 are essential for high fidelity simulations of intense laser propagation in optical set-ups [9], evaluation of material damage limits [10], development of supercontinuum sources [11] and post compression of short laser pulses [12]. A number of methods employing different flavours of z-scan [13,14], nonlinear interferometry [15–20], degenerate four-wave and nearly degenerate three–wave mixing [21–23], digital holography [24,25], spectrally resolved two-beam coupling [26] and frequency-resolved optical gating (FROG) [27] have been developed for characterization of nonlinear refraction of materials. To date, most of n_2 measurements have been carried out in the visible and near-infrared wavelength range and relatively few efforts were devoted for the determination of n_2 at wavelengths above 1.5 μm. With the exception of several works, where n_2 was evaluated by means of spectrally resolved two-beam coupling technique [28] and nonlinear foci position or four-wave mixing efficiency analysis [29,30], the majority of nonlinear refractive index measurements in crystals that are used in mid-infrared experimental set-ups have been performed by using z-scan [31–39]. This method is conceptually simple, however, the extraction of n_2 values usually requires some assumptions about the beam transverse mode and pulse shape (which are usually taken to be Gaussian). In practice, satisfactory fulfillment of these requirements quite often is problematic, especially in laser systems operating in the mid-infrared wavelength range. Accounting for experimental pulse characteristics and non-Gaussian beam propagation can be quite unpractical, as the wave-packet propagates through rather large distances of free space. Moreover, while the z-scan technique has a theoretical economic advantage in being able to operate using just a pair of single point detectors, its practical implementations are prone to experimental problems pertaining to the beam position and shape changes when the sample is moved through the laser focus. The illuminated sample area is not

#458850 https://doi.org/10.1364/OE.458850
Journal © 2022 Received 14 Apr 2022; revised 7 Jul 2022; accepted 21 Jul 2022; published 4 Aug 2022

Optics EXPRESS

constant throughout the measurement (and can be quite large at the positions outside the beam waist), which imposes strict requirements on the optical quality and clear aperture of the sample.

To address the mentioned issues, we have developed a variant of interferometric nonlinear refraction measurement technique, employing high quality microbolometric imaging detectors that have become accessible in the past decade. The method is based on Mach-Zehnder interferometer, one arm of which contains the sample being tested. Nonlinear refractive index values are calculated from the distortion of interference fringes caused by nonlinear refraction. Contrary to z-scan, the experiment does not require moving the sample; instead, it exploits the intensity variation across the beam profile as a source of intensity dependence. This provides spatially resolved measurements of nonlinear refraction, which allows one to catch the presence of unexpected effects, that could be overlooked when using techniques, based on single point detectors. Furthermore, a stationary imaged sample makes the accounting for experimental wave-packet parameters quite simple. Sample clear aperture of less than a millimeter in diameter is sufficient for n_2 measurements. Using the developed technique, we were able to collect reference n_2 data on a series of common optical materials used in mid-IR spectral range. We have determined the n_2 values at 1.03 μm, 2.2 μm and 3.2 μm. The measurements at 1.03 μm were performed in order to allow direct comparisons with available literature data. We discuss potential sources of errors in the obtained n_2 values, including, but not limited to, the influence of cascaded second-order nonlinearities [40].

2. Methods

One of the major effects of third-order nonlinearity is the intensity dependence of refractive index usually expressed as:

$$n(\mathrm{x},\mathrm{y},\mathrm{t}) = n_0 + n_2 I(\mathrm{x},\mathrm{y},\mathrm{t}), \tag{1}$$

where n_0 is the linear refractive index and $I(\mathrm{x},\mathrm{y},\mathrm{t})$ - spatio-temporal intensity profile of light. The constant n_2 in front of intensity is the nonlinear part of the refractive index. In the case of electronic polarization, the material response is instantaneous and local; therefore, the nonlinear change of n follows the intensity distribution across both laser beam and pulse profiles. It is convenient to define a total on-axis nonlinear phase shift at pulse peak acquired in a sample as:

$$B = \frac{2\pi}{\lambda}\int_0^L n_2 I_0(\mathrm{z})\mathrm{dz}, \tag{2}$$

where $I_0(\mathrm{z})$ - is the peak intensity at the propagation distance z, λ - wavelength, L - length of the medium and z - coordinate of the propagation axis. In case of a thin and non-absorbing sample the intensity profile can be considered constant and Eq. (2) can be rewritten simply as:

$$B = \frac{2\pi}{\lambda} n_2 I_0(0) L. \tag{3}$$

In this context a sample is considered thin, if the propagation of the pulsed beam through it does not result in the intensity change large enough to cause the B integral to alter <3% (when compared to the constant intensity case). After passing through such a sample without spatio-temporal coupling the nonlinear phase shift distribution for arbitrary shaped pulsed-beams can be expressed as:

$$\phi_{nl}(\mathrm{x},\mathrm{y},\mathrm{t}) = -B I^{\mathrm{xy}} I^{\mathrm{t}}, \tag{4}$$

where I^{xy} and I^{t} are, respectively, normalized to their maximum value (peak value is equal to 1) spatial and temporal intensity profiles of a pulsed-beam.

The induced nonlinear phase shift can be measured experimentally by means of interferometric techniques. The electric field of linearly polarized, amplitude and phase modulated light is given

Optics EXPRESS

by:

$$\mathcal{E} = \frac{1}{2} A \exp\left(i\omega_0 t - ik_0 \mathrm{z}\right) + \mathrm{c.c.} \tag{5}$$

Here ω_0 - carrier frequency, $k_0 = \frac{n_0 \omega_0}{\mathrm{c}}$ - wave number, c - speed of light in a vacuum, $A = a\exp(i\Phi)$ - slowly varying complex envelope, denoting spatio-temporal amplitude $a(\mathrm{x}, \mathrm{y}, \mathrm{t})$ and phase $\Phi(\mathrm{x}, \mathrm{y}, \mathrm{t})$ modulations. In Mach–Zehnder interferometer, the beam is split into sample and reference waves with complex envelopes A_{s0} and A_{r0}, correspondingly. The wave of the sample arm, assuming no transformation of the intensity profile and no losses due to absorption, after passing through the nonlinear medium is given as:

$$A_s = (1 - R) A_{s0} \exp\left(-iB I_{s_0}^{\mathrm{xy}} I_{s_0}^{\mathrm{t}}\right), \tag{6}$$

where R - reflection coefficient of a sample. The interference pattern at the output of the Mach-Zehnder interferometer can be obtained by crossing beams from sample and reference arms at a small angle γ. In case when A_s propagates perpendicularly to the XY plane of the detector and said waves are crossed in the XZ (here Z denotes the direction of the sample beam propagation) plane the projection of the reference wave to the XY plane can be written as:

$$A_r = A_{r0}\left(\mathrm{x}\cos\left(\gamma\right), \mathrm{y}, \mathrm{t}'\right) \exp\left(-ik_0 \sin\left(\gamma\right) \mathrm{x}\right). \tag{7}$$

Here $\mathrm{t}' = \mathrm{t} - \frac{\tan(\gamma)\mathrm{x}}{c}$ accounts for tilted pulse fronts of interfering waves. The phase factor corresponds to the phase difference of crossed wave fronts [20]. The net intensity distribution, recorded by the slow detector, is given by:

$$I_{net} = \frac{1}{2} \epsilon_0 c n_0 \int_{-\infty}^{+\infty} |A_s + A_r|^2 \, \mathrm{dt}. \tag{8}$$

In general, two overlapping laser pulses intersecting at an angle γ result in harmonically modulated spatial distribution of light in the plane of the detector, which can be qualitatively expressed as:

$$I_{net} \propto 1 + \cos\left(\frac{2\pi \mathrm{x}}{\lambda} \cdot \sin(\gamma) + \phi'_{nl}(\mathrm{x}, \mathrm{y})\right), \tag{9}$$

where $\phi'_{nl}(\mathrm{x}, \mathrm{y})$ is the phase modulation of the spatial interference pattern, caused by spatio-temporal SPM. At low light intensities, the nonlinear phase can be ignored and the interference patterns consist of straight parallel fringes with a constant spatial frequency determined by the intersection angle. At higher beam intensities, nonlinear refraction manifests itself as the distortion of the interference fringes, because the accumulated nonlinear phase has a maximum at the center of the laser beam and falls off in the periphery. This distortion can be quantified, thereby obtaining the nonlinear phase shift. With the energy of the used laser pulses known, Eq. (3) can then be used to evaluate n_2. In order to perform an accurate evaluation of n_2 we have recorded interference patterns at several distinct pulse energies E and used the entire accumulated data set for the determination of n_2 value.

The key steps of the retrieval of B value while accounting for the beam profile and pulse shape of the laser are illustrated in Fig. 1. The mean spatial phase difference between interfering waves over the entire beam cross section (Fig. 1(c)) is extracted from every measured interference image (Fig. 1(a)) using Fourier transform method (FTM) [41], carried out in two dimensions. Here the phase shift information is obtained by singling out the carrier spatial frequency shifted term of the Fourier spectrum (Fig. 1(b)). The resulting phase surface, corresponding to the effective total nonlinear phase shift B^{FTM}, is influenced by a number of factors, including the effect of interest, i.e. nonlinear refraction, but also linear phase shifts caused by tilted pulse fronts, diffraction, possible sample optical non-uniformity, small misalignment of the experimental

Optics EXPRESS

setup, etc. In order to account for these effects, the background phase distribution, corresponding to the effective total nonlinear phase shift $B_{\mathrm{ref}}^{\mathrm{FTM}}$ and obtained at low pulse energy (on average about 7 times smaller than the maximum E value), is subtracted from every calculated phase difference surface of a given sample. Note that there is no strict requirement to take this reference measurement in the complete absence of nonlinear refraction: initial phase may also contain some contribution of nonlinear refractive index. The *change* of total nonlinear phase $B^{\mathrm{FTM}} - B_{\mathrm{ref}}^{\mathrm{FTM}}$ remains proportional to the change in the laser pulse energy $E - E_{\mathrm{ref}}$, and can still be used to determine n_2. However, getting the data at lower intensities (and effectively extending the dynamic range of the experiment) is desirable because it greatly improves the measurement error. The middle part of the recovered wave front is fitted to the measured normalized sample beam profile I_s^{xy} (Fig. 1(d)). The full approximation is in the form of:

$$\phi'_{nl}(\mathrm{x},\mathrm{y}) = B_{\mathrm{eff}} I_s^{\mathrm{xy}} + K_x \mathrm{x} + K_y \mathrm{y} + C. \tag{10}$$

Here $B_{\mathrm{eff}} = B^{\mathrm{FTM}} - B_{\mathrm{ref}}^{\mathrm{FTM}}$ is an effective *change of* B, corresponding to the energy change $E - E_{\mathrm{ref}}$. Parameters K_x and K_y describe the tilt of the wave fronts in X and Y directions, whilst the C term is a constant phase offset. This fitting procedure is done for every pulse energy. Intensity-independent fit parameters are allowed to vary with differing E to account for the effects of uncontrolled linear phase shifts in the experiment, such as slight drift of beam direction. Each time the proportionality factor, relating B_{eff} and E, could be found from:

$$B_{\mathrm{eff}} = s_E(E - E_{\mathrm{ref}}). \tag{11}$$

In practice, the accuracy of Eq. (11) is increased by grouping all B_{eff} measurements of a given sample and finding s_E from a linear fit with a fixed intercept value of zero.

In addition to the spatial light distribution, the measured phase shift needs to be corrected to account for the influence of the actual pulse shape. The distortion of interference fringes follows the intensity envelope of the pulse, i.e. the interference pattern changes in time. However, the detector is slow compared to the femtosecond laser pulse and can only record time-averaged (blurred) interference patterns, resulting in B_{eff} value that is always smaller than B (with the exception of a non-realistic case of a pulse with rectangular intensity envelope). To find the relationship between the experimental time-averaged phase shift and the instantaneous phase change due to nonlinear refraction, we simulate interference images by using Eq. (8) with experimentally measured pulse shapes for a broad range of B. The precise spatial distribution is not important in this case, so we use the elliptical Gaussian function approximation. The B_{eff} is obtained the same way as before, by employing a surface fit of retrieved phase surfaces to Eq. (10). Figure 2 shows the results of numerical simulations for experimentally determined pulse shapes that were used for n_2 measurements presented further in the text. Evidently, for induced B values below 1.25 rad, this relationship can be satisfactorily approximated as linear:

$$B_{\mathrm{eff}} = s_B B. \tag{12}$$

Therefore, plugging the value of B_{eff} into Eq. (12) yields the value of B. Peak intensity, required for the absolute n_2 evaluation, was calculated by using:

$$I_0 = \frac{E}{J}, \tag{13}$$

where $J = \iiint I^{\mathrm{xy}} I^{t} dxdydt$ is a numerical integral of normalized experimentally measured beam and pulse intensity profiles I^{xy} and I^{t}. Finally, from Eq. (3), Eq. (11), Eq. (12), and Eq. (13) we get the final expression for the nonlinear refractive index:

$$n_2 = \frac{\lambda}{2\pi L} \frac{s_E}{s_B} J. \tag{14}$$

Optics EXPRESS

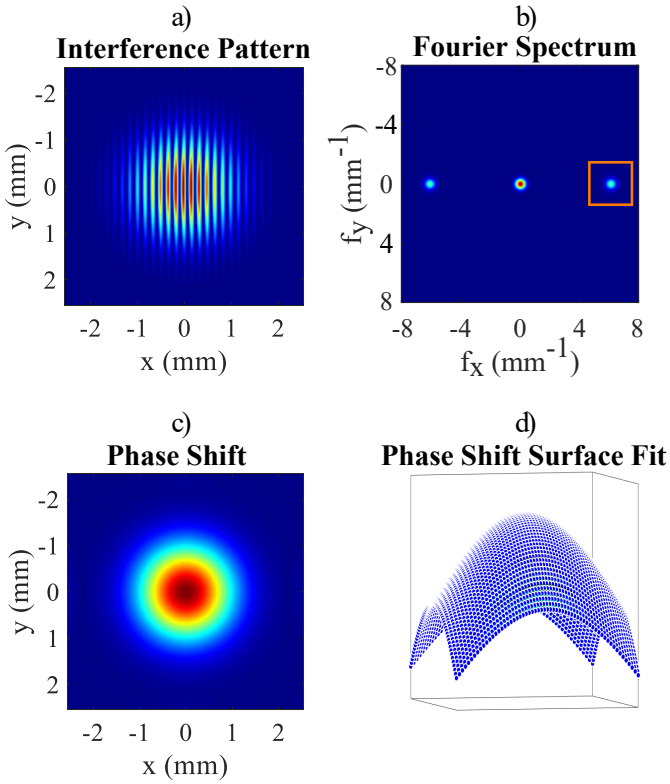

Fig. 1. Visual representation of the effective total nonlinear phase shift retrieval sequence from the interference image.

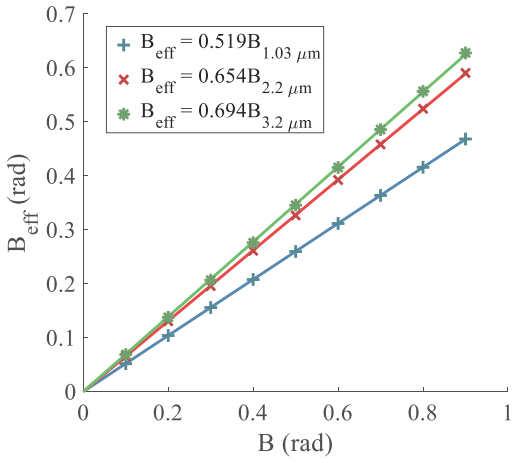

Fig. 2. Calculated relationships between measured effective total nonlinear phase shift and set total nonlinear phase shift values for experimentally determined pulse shapes at different wavelengths used in the n_2 measurements. Dots – calculated points, lines – linear fit.

Optics EXPRESS

3. Experiment

The layout of our experimental set-up based on Mach-Zhender interferometer is presented in Fig. 3. The mid-IR pulses were produced by home built optical parametric amplifier (OPA), pumped by femtosecond Yb:KGW laser ("Pharos", "Light Conversion"). The OPA generates pulses of 2.2 μm and 3.2 μm central wavelength with the energy of up to 40 μJ at 1 kHz repetition rate. For the measurements at 1.03 μm, properly attenuated fundamental wave of the Yb:KGW laser was used. The light beam entering the interferometer is split by using a $\approx$ 4 mm thick CaF_2 beamsplitter (BS) and the transmitted beam is focused into the sample using a spherical mirror SM1 (focal length f = 400 mm). In case of 1.03 μm we replaced SM1 with a flat mirror and used a misaligned telescope for focusing. Then two lenses were added to the reference arm, to collimate the beam. The full beam waist at e^{-2} level varied between 0.62 mm and 0.94 mm for different pump wavelengths and the Rayleigh length, assuming perfect Gaussian beams, exceeded 100 mm in all cases. The thickness of all investigated media was below 21 mm, therefore the beam propagating in the sample can be considered quasi-parallel. In addition, the values of B integral roughly did not exceed 1 rad in all experiments and no discernible self-focusing was observed. Therefore, the beam profile can be considered constant throughout the entire sample. In order to avoid diffraction effects, the end of the sample was imaged onto the beam profiler (BP) using spherical mirrors SM2 (f = 100 mm) and SM3 (f = 500 mm), resulting in 5x overall magnification. To approximately match the beam intensities in the sample and reference arms, a Fresnel reflection off a fused silica wedge (W) was utilized in the sample arm.

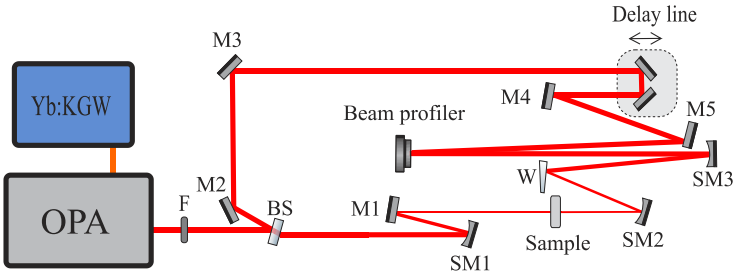

Fig. 3. Optical layout of n_2 measurement setup. BS - beamsplitter, M - flat mirror, SM - spherical mirror, F - neutral density reflective filter, W - wedge shaped prism.

The beam reflected from BS was directed to the reference arm and its optical path length was matched to the one of the sample arm by adjusting the delay line. The beams from sample and reference arms were superimposed on the sensor of BP. The microbolometric camera ("Dataray", 640x480 pixel matrix with 0.017 mm pixel pitch) was employed for the measurements at 2.2 μm - 3.2 μm, while a CMOS beam profiler ("Cinogy Technologies", 2040x2040 matrix and 0.0055 mm pixel pitch) was used for n_2 measurements at 1.03 μm. In our experiments $\gamma \approx 1°$, which have meant that with this set-up we resolved the spatial period of the fringes with $\approx$ 10 points. The pulse energy in both arms was varied by means of the variable neutral density filter (or the half-wave plate and a polarizer for 1.03 μm experiments) placed at the OPA output and measured using a thermal power meter (Ophir Vega with sensor 2A-SH).

To address the scarcity of available n_2 data in the infrared spectral range, we measured 15 different infrared optical materials, also varying the polarization direction for birefringent samples. A complete list of investigated samples and their properties is presented in Table 1. ZnSe and ZnS ("Cleartran") samples are polycrystalline, SBN-61 is polydomain, KRS-5 and KRS-6 are mixed crystals, while UVFS is amorphous. The remaining samples are monocrystalline. For the samples with known orientation, we also presented the polar angle θ and the azimuthal angle φ of the cut.

Optics EXPRESS

Table 1. Samples and their properties.

Sample	Orientation	Thickness, mm
GaSe	$\theta = 0°$, $\mathcal{E} \parallel$ X	0.56
AGS ($AgGaS_2$)	$\theta = 39°$, $\varphi = 45°$	0.98
ZGP ($ZnGeP_2$)	$\theta = 74°$, $\varphi = 0°$	0.72
SBN-61 ($Sr_{0.61}Ba_{0.39}Nb_2O_6$)	$\theta = 90°$, $\varphi = 0°$	5.05
KTA ($KTiOAsO_4$)	$\theta = 45°$, $\varphi = 0°$	5.065
LGS ($LiGaS_2$)	$\theta = 45°$, $\varphi = 0°$	8.195
BGSe ($BaGa_4Se_7$)	$\theta = 0°$	1.785
GaAs	(100)	0.50
Si	unknown	1.04
ZnTe	unknown	0.63
ZnS		6.125
ZnSe		2.04
KRS-5 (TlBr-TlI)		4.01
KRS-6 (TlBr-TlCl)		1.7
UVFS (SiO_2)		20

The examples of X and Y cuts of the phase shifts (ϕ'_{nl} (x, y)) retrieved from the interference patterns for different absolute pulse energies in the sample along with corresponding approximations are shown in Fig. 4, whilst such data for all investigated samples and conditions is available in Supplement 1 (Figs. S5–S16), along with examples of experimental interferometric images (Figs. S18–S20). Here, wave front tilt (K_x and K_y) and constant (C) terms are subtracted to aid the comparisons. To estimate pulse energy within the medium, we quantified the sample reflection coefficient. For every instance we made two energy measurements: with and without the sample. We assumed that R for each surface is the same. The fit range (illustrated by the vertical dashed lines in Fig. 4) in the X and Y directions for the different samples and wavelengths varied from ±0.5 mm to ±0.8 mm, which corresponds to 30% - 46% of the beam diameter in every case. It was chosen arbitrary by considering a trade-off between the number of included points and visually estimated goodness of fit. The choice was held for all measurements of a certain wavelength and/or beam size. While the approximation matches experimental data within the chosen fitting range, clear deviations could sometimes be observed outside these limits. As a rule, the correspondence between the data and the model improves with the increase of induced maximum phase shift. Discrepancies outside the fitting range may occur as a consequence of crossed pulse fronts, errors in the background phase surface measurement, apodization artefacts in FTM, sample surface quality, insufficient signal-to-noise ratio and uncontrolled factors like residual air turbulence or beam pointing instabilities.

Fig. 5 presents the extracted effective total phase shift dependence on the pump pulse energy for the several samples. Identical data for all performed measurements is available in Supplement 1 (Figs. S1–S4). The linear relationship between the induced phase shift and pulse energy with low data scattering and zero offset indicates the robustness of the measurement and numerical procedures.

Accurate n_2 evaluation using proposed method requires precise knowledge of pulse parameters, therefore we have measured the amplitude and phase characteristics of the mid-IR pulses at the output of OPA using sum-frequency generation (SFG) cross-correlation frequency-resolved optical gating (XFROG) [42]. The 1.03 μm Yb:KGW laser pulse characterized by second-harmonic generation (SHG) FROG technique [43,44] was used as a reference pulse in the XFROG

Optics EXPRESS

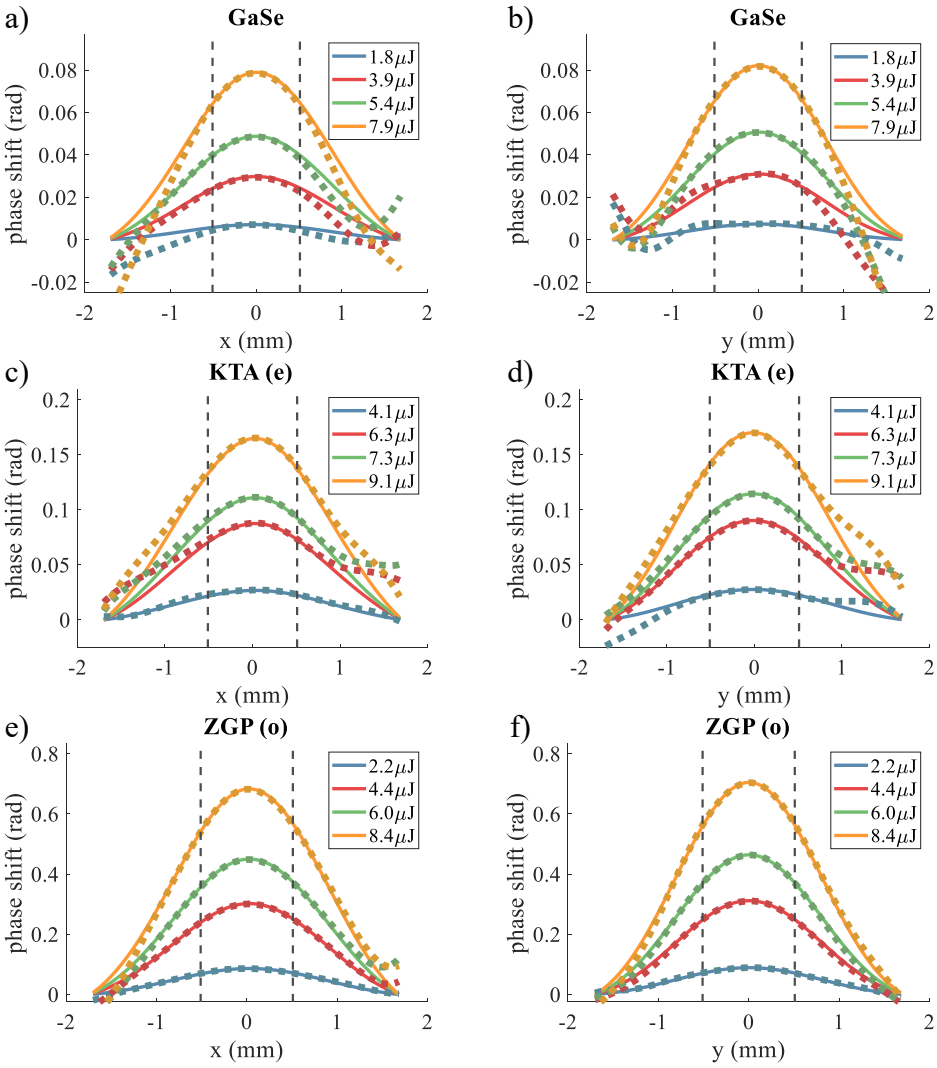

Fig. 4. Retrieved X and Y cuts of phase shifts observed in GaSe (a),(b), KTA (c),(d), ZGP (e),(f) for various laser pulse energies at 3.2 μm. Dashed line - data, solid line - approximation. The vertical dashed lines indicate the part of the data included in n_2 estimation.

Optics EXPRESS

set-up. The measurement results give the values in vicinity of 230 fs, 170 fs and 190 fs for 1.03 μm , 2.2 μm and 3.2 μm pulses, respectively. Typical pulse characteristics can be found in Supplement 1 (Fig. S17). It must be noted, that the sample beam propagates through additional 4 mm of CaF_2 in the beamsplitter plus the beams of both arms propagate through 2 mm thick filter F and the combined 1.6 mm thickness of CaF_2 collimating lenses (collimating the output of OPA and not shown in Fig. 3), which were also employed for focusing during 1.03 μm measurements. The numerical modeling using full n_0 dispersion relations from Sellmeier equations indicates that such dispersive propagation changes the pump pulse duration by up to 16%. Propagation effects on the pulses were directly included in the model when calculating peak intensity: the pulses as measured by (X)FROG were first numerically propagated through the transmissive components, and only then used in the numerical simulations of interference patterns. It was assumed, that neither of the wave-packets have spatio-temporal couplings. As a result, the correction factor s_B (see Eq. (12)) was extracted, enabling pulse shape correction of the determined nonlinear phase shift (see Fig. 2).

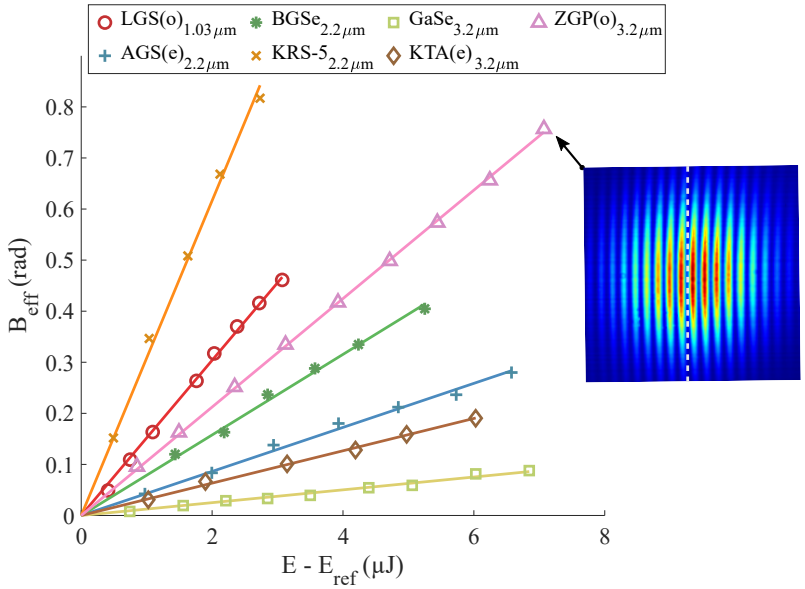

Fig. 5. Effective total nonlinear phase shift at different energies within the sample. Dots – experimental points, lines – linear fits. The raw interference image, obtained during ZGP (o) measurement at maximum energy, is shown in the inset.

The data presented in Fig. 5 and Fig. 2 was then used to calculate the absolute value of nonlinear refractive index using Eq. (14). Complete information about the peak intensities and E_{ref} used in different experiments can be found in Supplement 1 Table S1 and Table S2, respectively. We have estimated by numerical simulations that in perfect experimental conditions we could still reliably detect nonlinear phase shifts of the $\approx 10^{-7}$ rad order of magnitude and we could still sense $B_{\text{eff}} = 10^{-8}$ rad with the accuracy of about 16% (see Fig. S23). However, in the presence of noise this limit is pushed to about 10 mrad (see Fig. S24). In some cases we can still retrieve $B_{\text{eff}} = 10$ mrad with the error of about 8%, when the noise to signal amplitude ratio is 10%. However, the error tends to depend on the actual random manifestation of the noise, meaning, that this inaccuracy could randomly increase to about 30%. Nevertheless, $B_{\text{eff}} \approx 10$ mrad seems to be the lower limit, when using our set-up (with microbolometric beam profiler) and the detector's noise to signal amplitude ratio is around 2% or higher.

Optics EXPRESS

4. Results and discussion

To be able to make direct comparisons of determined n_2 values with literature data, we performed n_2 measurements on UVFS and several nonlinear crystals at 1.03 μm, the wavelength at which experimental data is abundant. Table 2. compares the measured values of the effective nonlinear refractive index n_2^{eff} with previously determined values from scientific literature. We can safely ignore the effects of diffraction and self-focusing as the Rayleigh length is large when compared to the sample thickness and B is generally small. However, by performing linear pulse propagation simulations in every sample we have found that, in some cases, the drop of pulse peak intensity due to sample dispersion is non-negligible and leads to the change of calculated n_2 value up to 10%. To account for this phenomena at certain central wavelengths we calculated the correction for B by direct numeric integration as per Eq. (2). Such corrections were employed for KTA, LGS, SBN-61, ZnS, ZnSe at 1.03 μm and for KTA, SBN-61 at 3.2 μm. Overall, our results are in a good agreement with n_2^{eff} values presented in scientific literature. Note, that the agreement of the values holds out for media with n_2^{eff} covering the range of almost two orders of magnitude (see results for UVFS and ZnSe), providing further confidence in the validity of our method. Importantly, the n_2^{eff} values measured at 1.03 μm consistently matched the earlier works regardless of the fact that the thickness of used samples varied from 2 mm (ZnSe) to 20 mm (UVFS). This, along with the fact that the measurements were carried out on a stationary sample (hence looser focusing conditions had no side effect to the quality of the experiment) is a significant practical advantage, especially when investigating exotic materials, where making a sample dedicated solely for n_2^{eff} measurement may be prohibitively expensive. A slight difference in n_2^{eff} for ordinary (o) and extraordinary (e) waves in KTA and LGS was observed, however, this difference is within the limits of experimental error. When measuring ZnSe and ZnS we visually observed the second-harmonic (SH) signal, which is a known consequence of random quasi-phase-matching in these materials [51]. The random nature of this process led to the appearance of noticeable noise in the transmitted beam profiles, presumably due to random variation of quasi-phase-matched SHG efficiency over the beam area. Nevertheless, we believe that this have little impact on our measurements since the estimated fraction of energy converted to SH is of the order of a few percent.

Table 2. The n_2 results at 1.03 μm.[a]

Material	n_2^{eff} (this work)	n_2^{eff} (literature)
KTA (o)	**0.185 ± 0.023**	[b]$0.17 \pm 0.03_{(0.78\mu\text{m})}$[45,46]
KTA (e)	**0.17 ± 0.03**	[b]$0.15_{(1.03\mu\text{m})}$[47]
LGS (o)	**0.45 ± 0.06**	[b]$<0.64_{(1.03\mu\text{m})}$[48]
LGS (e)	**0.41 ± 0.05**	[b]$0.41_{(1.03\mu\text{m})}$[47]
SBN-61 (o)	**0.61 ± 0.07**	$0.524_{(1.06\mu\text{m})}$[49]
		$0.44 \pm 0.07_{(1.2\mu\text{m})}$[29]
ZnS	**0.68 ± 0.08**	$0.84_{(1.06\mu\text{m})}$[49]
ZnSe	**2.31 ± 0.35**	$2.87_{(1.06\mu\text{m})}$[49]
UVFS	**0.0253 ± 0.0032**	$0.0274 \pm 0.0017_{(1.053\mu\text{m})}$[50]

[a]All n_2 values are in units of $10^{-14}\,\frac{\text{cm}^2}{\text{W}}$.
[b]Same value for both polarization modes.

The measurements performed at 2.2 μm and 3.2 μm wavelengths provided hitherto scarce n_2^{eff} data on infrared optical media, including narrow band gap solids. The measurement results are presented in Table 3, where we also compare the obtained n_2^{eff} values to the results reported in

Optics EXPRESS

literature at wavelengths above 2 μm. While most of the determined n_2^{eff} values obtained in our measurements are similar to those published in scientific literature, the n_2^{eff} values measured for KRS-5, KRS-6, ZGP (for e polarization), GaSe and Si deviate significantly from earlier works. Possible reasons for such deviations include different wavelengths and sample orientations, i.e. parameters defining the effective third-order susceptibility $\chi_{\text{eff}}^{(3)}$ (here and on the nonlinearity of interest is $\chi^{(3)}(\omega;\omega,\omega,-\omega)$). In non-centrosymmetric crystals, an additional source of n_2^{eff} uncertainty is the cascaded second-order nonlinearities that can induce additional nonlinear refraction, which can exceed the cubic nonlinearity in magnitude and may have an opposite or identical sign [40]. The only centrosymmetric materials investigated here are Si, KRS-5, KRS-6 and UVFS. For all other investigated media, the dominant cascaded second-order process was phase-mismatched SHG and the corresponding cascaded n_2 part can be calculated as follows [40]:

$$n_2^{\text{casc}} = -\frac{4\pi}{c\epsilon_0\lambda}\frac{d_{\text{eff}}^2}{n_{2\omega}n_\omega^2\Delta k}. \tag{15}$$

Here n_ω - refractive index of the fundamental wave, $n_{2\omega}$ - refractive index of the second-harmonic wave, d_{eff} - effective second-order nonlinearity for a given SHG process type and $\Delta k = k(2\omega) - 2k(\omega)$ - phase mismatch. The d_{eff} expressions for a given crystal class and process type of the uniaxial crystals were taken from [53]. For mm2 biaxial crystals (KTA and LGS) we derived d_{eff} expressions using the formalism presented in [54]. We have skipped the n_2^{casc} calculation for ZnS, ZnSe and SBN-61 samples because of polycrystalline or polydomain structure of these materials. Furthermore, we did not calculate contribution of cascaded processes to measured n_2 for BGSe, GaAs and ZnTe due to lack of full information on crystal orientation of the available samples. GaSe belongs to 6m2 crystal class and for $\theta = 0°$ cut samples and *o*-polarized pump the oo-o and oo-e frequency doubling processes should be accounted for. AGS and ZGP are $\bar{4}$m2 symmetry class crystals. Therefore, depending on the φ value, the oo-e process type for the *o*-polarized incident wave or ee-o and ee-e process types for the *e*-wave were evaluated when performing n_2^{casc} calculation for these crystals. The evaluation of d_{eff} for GaSe, AGS and ZGP samples was performed using values of second-order nonlinear coupling tensor elements (d_{ij}) taken from [55]. For KTA and LGS crystals, the nonzero contribution to d_{eff} were found for oo-e and ee-e types of interaction for o and e polarized pump, respectively. The d_{eff} for KTA and LGS was calculated using d_{ij} values presented in [56,57]. In all the cases d_{ij} values were scaled to the experimental wavelengths by using the Miller's rule [58]. The n_2 values measured in our experiments with subtracted n_2^{casc} contribution (n_2^{Kerr}) are presented in Table 4. The last column of the table contains n_2^{Kerr} values that we calculated using the data from other published works.

Since the presented method relies on the measurements of interference-modulated beam profiles, it is perhaps unsurprising that its results are sensitive to the optical surface quality of the samples. We have found, that in cases where the experiments are performed on samples with optical or mechanical damage, the obtained n_2^{eff} values can be wrong, often without any indication in the quality of the fits. As can be expected, such errors tended to decrease with increased wavelength. The ilustration of interference patterns, recorded using different quality samples, is presented in Supplement 1 (Fig. S21). On the other hand, the presented technique has an advantage of being able to work on low aperture samples, with the beam size on the sample small and kept constant throughout the measurement. The method also turned out to be robust to small clipping of the peripheral part of the measuring beam: as long as the central part of the beam was on an optically clear sample, the resulting n_2 values did not change. It was tested by measuring two different samples of GaSe. In one case the beam was slightly clipped because of small clear aperture (data not shown) and the resulting n_2 value did not change. However, the

Optics EXPRESS

Table 3. The n_2 results at 2.2 μm and 3.2 μm.[a]

Material	n_2^{eff} at 2.2μm	n_2^{eff} at 3.2μm	n_2^{eff}
	(this work)	(this work)	(literature)
GaSe	**2.14 ± 0.34**	**0.71 ± 0.1**	$2.1 \pm 1.3_{(10\mu\text{m})}$ [30]
AGS (o)	**1.95 ± 0.35**	**1.99 ± 0.37**	$1.5 \pm 0.2_{(4.65\mu\text{m})}$ [33]
AGS (e)	**2.29 ± 0.42**	**1.37 ± 0.18**	$1.6 \pm 0.3_{(4.65\mu\text{m})}$ [33]
ZGP (o)	**5.99 ± 0.99**	**4.4 ± 0.61**	$5.5 \pm 0.6_{(2.2\mu\text{m})}$ [33]
			$5.3 \pm 0.8_{(4.7\mu\text{m})}$ [33]
ZGP (e)	**7.1 ± 0.88**	**1.02 ± 0.3**	$5.1 \pm 0.7_{(2.2\mu\text{m})}$ [33]
			$6.3 \pm 0.9_{(4.7\mu\text{m})}$ [33]
SBN-61 (o)	**0.87 ± 0.13**	**0.58 ± 0.09**	$0.81 \pm 0.23_{(2\mu\text{m})}$ [29]
			$1 \pm 0.15_{(2.4\mu\text{m})}$ [29]
KTA (o)	**0.22 ± 0.03**	**0.22 ± 0.03**	
KTA (e)	**0.13 ± 0.02**	**0.22 ± 0.05**	
LGS (o)	-	**0.56 ± 0.1**	
LGS (e)	**0.57 ± 0.08**	**0.48 ± 0.08**	
GaAs	-	**8.56 ± 1.2**	$13 \pm 3.25_{(3.9\mu\text{m})}$ [36]
BGSe	**1.96 ± 0.4**	**0.95 ± 0.18**	
Si	**7 ± 1.14**	**4.54 ± 0.64**	$\approx 10.4 \pm 2_{(2.2\mu\text{m})}$ [32]
			$7.7 \pm 1.54_{(2\mu\text{m})}$ [36]
			$11 \pm 2.75_{(3.9\mu\text{m})}$ [36]
ZnS	**0.74 ± 0.1**	**0.6 ± 0.09**	$0.55 \pm 0.11_{(2\mu\text{m})}$ [36]
			$0.478 \pm 0.05_{(2.3\mu\text{m})}$ [28]
			$0.5 \pm 0.125_{(3.9\mu\text{m})}$ [36]
			$0.455 \pm 0.05_{(3.5\mu\text{m})}$ [28]
ZnTe	**3.01 ± 0.41**	**1.32 ± 0.21**	
ZnSe	**1.59 ± 0.24**	**1.22 ± 0.21**	$1.5 \pm 0.3_{(2\mu\text{m})}$ [36]
			$1.13 \pm 0.12_{(2.3\mu\text{m})}$ [28]
			$1.2 \pm 0.3_{(3.9\mu\text{m})}$ [36]
			$1 \pm 0.11_{(3.5\mu\text{m})}$ [28]
KRS-5	**2.6 ± 0.59**	**2.14 ± 0.32**	$1.05 \pm 0.19_{(3.1\mu\text{m})}$ [52]
KRS-6	**1.21 ± 0.27**	**1.19 ± 0.19**	$0.54 \pm 0.1_{(3.1\mu\text{m})}$ [52]

[a]All n_2 values are in units of $10^{-14}\,\frac{\text{cm}^2}{\text{W}}$.

Optics EXPRESS

Table 4. The n_2^{eff} values with excluded n_2^{casc}.[a]

Material	n_2^{Kerr} $_{(1.03\mu\text{m})}$	n_2^{Kerr} $_{(2.2\mu\text{m})}$	n_2^{Kerr} $_{(3.2\mu\text{m})}$	n_2^{Kerr}
	(this work)	(this work)	(this work)	(literature)
GaSe		**3.52 ± 0.66**	**3.47 ± 1.13**	$4.31 \pm 1.58_{(10\mu\text{m})}$ [30]
AGS (o)		**2.13 ± 0.36**	**1.36 ± 0.42**	$1.22 \pm 0.22_{(4.65\mu\text{m})}$ [33]
AGS (e)		**2.49 ± 0.43**	**1.71 ± 0.21**	$1.98 \pm 0.32_{(4.65\mu\text{m})}$ [33]
ZGP (o)		**5.99 ± 0.99**	**4.4 ± 0.61**	$5.5 \pm 0.6_{(2.2\mu\text{m})}$ [33]
				$5.3 \pm 0.8_{(4.7\mu\text{m})}$ [33]
ZGP (e)		**7.6 ± 0.88**	[b] **5.44 ± 0.95**	$5.58 \pm 0.71_{(2.2\mu\text{m})}$ [33]
KTA (o)	**0.19 ± 0.02**	**0.22 ± 0.03**	**0.23 ± 0.03**	$0.15_{(1.03\mu\text{m})}$ [47]
KTA (e)	**0.23 ± 0.03**	**0.26 ± 0.02**	**0.3 ± 0.05**	$0.2_{(1.03\mu\text{m})}$ [47]
LGS (o)	**0.46 ± 0.06**		**0.49 ± 0.1**	$0.42_{(1.03\mu\text{m})}$ [47]
LGS (e)	**0.42 ± 0.05**	**0.59 ± 0.08**	**0.5 ± 0.08**	$0.41_{(1.03\mu\text{m})}$ [47]

[a]Calculated for various measurements. All n_2 values are in units of $10^{-14}\frac{\text{cm}^2}{\text{W}}$.
[b]Calculated numerically by simulating the propagation of the measured pulse.

beam in presented measurements was not clipped as the apertures of the samples are significantly larger than the beam diameter.

The results presented in Tables 2, 3, and 4 exhibit several interesting features. For generality we have compared our n_2^{Kerr} (or n_2^{eff} if not available otherwise) data to the two-band model [49,59] in Supplement 1 (Fig. S22). We used various suggested parameters [49,60]. Some points did not agree with the theoretical tendency well. This can be explained by indirect band gap, cascaded second-order processes and complicated band structure. Nevertheless, we believe that the remaining discrepancy can be further corrected by using different band gap energy E_g values, since they vary in the scientific literature and $n_2 \propto E_g^{-4}$. It seems that SBN has an additional peak of n_2^{eff} far from two-photon absorption (2PA) cut-off wavelength between 1 μm and 3 μm. Also, it is evident that n_2^{casc} is rather insignificant (in comparison to n_2^{eff}) for the presented cases of LGS measurements. We skipped the LGS (o) measurement at 2.2 μm because the experimental conditions were too close to phase matched SHG. For KTA pumped by the *e*-wave, the cascaded contribution is quite large. This can explain the anomalous n_2^{eff} value at 2.2 μm. Both of these mm2 crystals exhibit a slightly larger n_2^{Kerr} value for the *e*-wave, however, the differences are still within the error bounds of the measurement. When looking at AGS and ZGP samples at both wavelengths it is clear that n_2^{Kerr} differs for different polarizations. This could be explained by the fact, that for $\bar{4}$m2 crystals and *e*-waves $\chi_{\text{eff}}^{(3)}$ depends on more tensor elements than for *o*-waves. Furthermore, for AGS and ZGP the n_2^{casc} at 2.2 μm is quite low, while for GaSe it has a negative sign and large absolute value. Interestingly, for GaSe the n_2^{eff} decreased substantially with increased wavelength, but this decrease was almost entirely due to stronger negative cascaded contribution, while the value of n_2^{Kerr} was nearly identical for both wavelengths. The values of n_2^{Kerr} determined for AGS at both polarizations differ significantly from those provided in the literature. Given that the polar angle of the samples used in our measurements differs only by 1° from the referenced work [33], the observed discrepancy is most likely due to significant difference in the pump wavelength. In contrast, for ZGP samples at 2.2 μm the notable n_2^{Kerr} distinction is observed only for the *e*-wave. Here, the source of discrepancy may have been the difference in polar angle.

At 3.2 μm, we have observed a large difference between n_2^{eff} values in ZGP for different polarizations. This can be fully explained by the large negative n_2^{casc} contribution. Unfortunately,

Optics EXPRESS

in this case the Eq. (15) is not applicable because of small phase mismatch and significant fundamental wave depletion. Therefore, we had to evaluate the n_2^{casc} by numerically simulating the propagation of a measured pulse in ZGP crystal. Notice, that for ZGP (o) $n_2^{\text{casc}} = 0$, because $d_{\text{eff}} = 0$ for oo-e process and $\varphi = 0°$. Also, the agreement of n_2^{eff} values is rather good for o-waves, because $\chi_{\text{eff}}^{(3)}$ does not depend on θ. In fact, when $\varphi = 0°$ $\chi_{\text{eff}}^{(3)}$ consists of only 1 tensor element. Therefore, for this propagation direction and o polarization n_2^{eff} represents $\chi_{\text{xxxx}}^{(3)}$ tensor element. The same is true for the n_2^{Kerr} values of GaSe when using the o-wave, since $\chi_{\text{eff}}^{(3)}$ is also independent of propagation direction.

To further investigate the influence of cascaded second-order nonlinearity on the nonlinear refraction, we performed the measurements of n_2 at different polar angles in AGS and compared them with the prediction of Eq. (15) in Fig. 6. We used n_2^{Kerr} value from Table 4. as a third-order n_2 contribution. As one can see, the formula predicts the experimental values quite well when pump propagation angle is far from SHG phase matching (in our case when detuning is $> \approx 1.5°$). However, around the phase-matching angle ($\approx 35.3°$ at 3.255 μm), the discrepancies become more pronounced. This can be expected as the assumptions of Eq. (15) are not valid anymore, plus the fundamental wave begins to suffer from losses, caused by efficient conversion, thereby increasing the error of n_2^{eff} calculation.

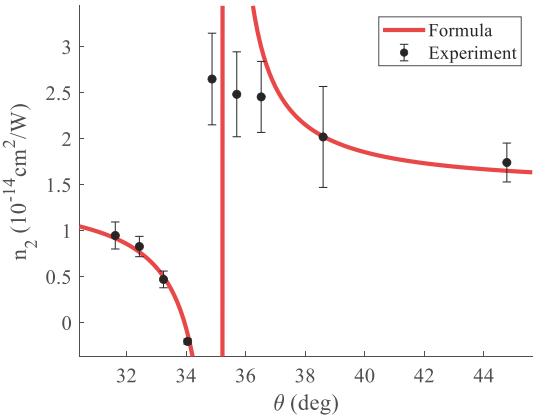

Fig. 6. Nonlinear refractive index as a function of internal polar angle for AGS (o) at 3.2 μm.

Data, colected on n_2 in Si and GaAs pumped by 2.2 μm pulses, presented additional interpretation difficulties. The function of $B_{\text{eff}}(E - E_{\text{ref}})$ was no longer linear, indicating that the nonlinear phase was no longer a linear function of light intensity. For Si this problem could be addressed by taking into account the 2PA effect. We measured the normalized transmittance T of the sample as a function of energy (see Fig. 7) and retrieved the 2PA coefficient $\beta_{\text{2PA}} = 0.238$ $\frac{\text{cm}}{\text{GW}}$ by numerically fitting the experimental data points to the model:

$$I(E, \text{x}, \text{y}, \text{t}, \text{z}) = \frac{I(E, \text{x}, \text{y}, \text{t}, 0)}{1 + I(E, \text{x}, \text{y}, \text{t}, 0) \cdot \beta_{\text{2PA}} \cdot \text{z}}, \tag{16}$$

$$T = \frac{\iiint I(E, \text{x}, \text{y}, \text{t}, L) dxdydt}{E} \cdot \frac{E_{\text{min}}}{\iiint I(E_{\text{min}}, \text{x}, \text{y}, \text{t}, L) dxdydt}, \tag{17}$$

where E_{min} is the lowest E value used in this experiment. The determined β_{2PA} value was close to the one reported in literature [32]. Then we accounted for 2PA by correcting B values while performing the linear fit of a function $B(E - E_{\text{ref}})$ (see section "Methods"). The mentioned

Optics EXPRESS

procedure was performed for low E values, where the relationship $B(E - E_{\text{ref}})$ is still close to linear. The corrected value of n_2^{eff} was found to be $\approx 0.5 \cdot 10^{-14}$ $\frac{\text{cm}^2}{\text{W}}$ higher in comparison to the value calculated without taking 2PA into account. This adjustment is included in the final result, presented in Table 3.

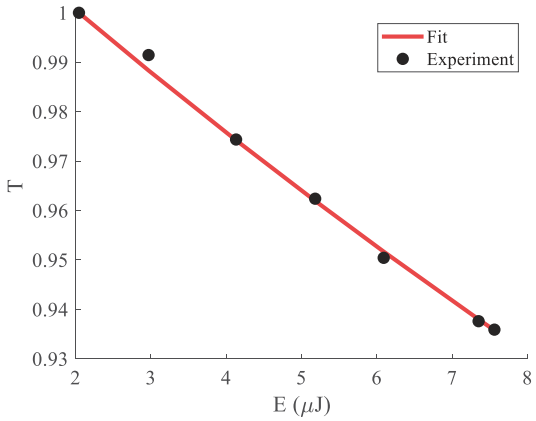

Fig. 7. Normalized transmittance measurement of Si at 2.2 μm.

In the measurements on Si sample, all the phase shift surfaces were qualitatively similar to the ones shown in Fig. 4, i.e., they had the shape of the measured beam profile. This turned out not to be the case for GaAs. Figure 8 presents the retrieved phase shift profile in the y coordinate as a function of beam incident peak intensity within the sample as well as the variation of B_{eff} value measured at the beam center for different pump energies. The surface plot presented in Fig. 8 was constructed by interpolating the measured data taken at 11 different intensity values. At low peak intensities (up to 3 $\frac{\text{GW}}{\text{cm}^2}$), the phase shift resembles the beam profile, and B_{eff} increases with pulse energy, however, this relationship is no longer linear. When increasing pump intensity, the phase shift in the center saturates and begins to decrease resulting in non-monotonous toroidal-like nonlinear lens. Moreover, B_{eff} reaches 0 at about 5.5 $\frac{\text{GW}}{\text{cm}^2}$. By further increasing pulse energy the SPM in the center of the beam reverses its sign, which corresponds to a defocusing wave front. At the highest intensity of 7.7 $\frac{\text{GW}}{\text{cm}^2}$ we retrieved that $B_{\text{eff}} = -1.1$ rad. There are several candidate mechanisms that could cause a defocusing SPM: three-photon absorption (3PA)-induced plasma generation, impact ionization via intrinsic carriers and cascaded SHG. Including such effects in direct propagation model may be possible, but is beyond the scope of the present study. We hypothesize, that the full explanation of observed nonlinear refraction in GaAs could lie in additional effects such as 2PA from one second-harmonic photon and one fundamental photon or higher-order Kerr effect. However, it is important to note that the presented method does clearly signal about such irregularities in the intensity dependent data shown in Fig. 8. This creates the opportunity to use the experimental information for unraveling the underlying mechanisms of nonlinear refraction and in principle enables the measurements of spatially resolved n_2, useful for specially tailored materials. In contrast, such subtleties might be harder to observe in other n_2 measurement techniques that employ single point detectors. This is especially true when working outside the visible range, where non-trivial intensity-dependent beam profile transformations, caused by exotic phase fronts, similar to the ones shown in Fig. 8(a), are easy to miss.

Optics EXPRESS

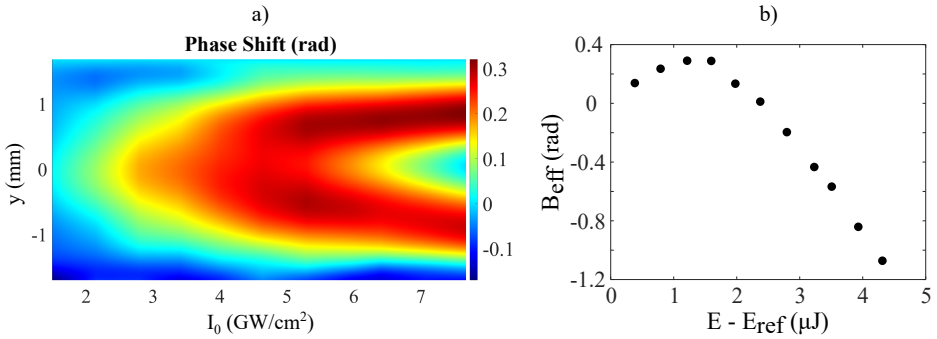

Fig. 8. The GaAs n_2 measurement at 2.2 μm. (a) Intensity dependence of y-profile of nonlinear phase shift induced in GaAs; (b) dependence of retrieved accumulated nonlinear phase on incident pulse energy.

5. Conclusion

We have presented a newly developed interferometric technique for the measurement of nonlinear refractive index, which allows directly accounting for the spatio-temporal parameters of the measuring laser pulses. In addition, the method enables nonlinear refraction measurements without mechanically moving the sample, and sub-millimeter diameter optically clear aperture is sufficient for accurate determination of n_2. We employed this technique to collect hitherto scarce n_2 data on a series of infrared optical media using 2.2 μm and 3.2 μm wavelengths. The obtained n_2 values were in good agreement with available literature values. Collected data also revealed significant influence of cascaded second-order nonlinearities on the resulting value of nonlinear refractive index in non-centrosymmetric optical media. Additional bonus of the presented n_2 measurement procedure lies in the direct measurements of laser beam inteference patterns using high quality microbolometric imaging detectors that have emerged in the past decade. Beam profile and interference data that can be internally checked for experimental consistency (e.g. optical quality of the sample, beam clipping, etc.,), which facilitates accurate spatially resolved measurements of nonlinear optical properties in mid-IR, where the traditional methods are prone to error and the data on the material properties is still scarce.

Funding. European Regional Development Fund (01.2.2-LMT-K-718-01-0014); Laserlab-Europe (EU-H2020 871124).

Acknowledgments. We would like to thank Assoc. Prof. Gintaras Tamošauskas for BGSe, ZnTe, and KRS-6 samples and Daugirdas Kuzma along with "Eksma Optics" for the ZGP sample.

Disclosures. The authors declare no conflicts of interest.

Data availability. Data underlying the results presented in this paper are not publicly available at this time but may be obtained from the authors upon reasonable request.

Supplemental document. See Supplement 1 for supporting content.

References

1. X. Zou, W. Li, S. Qu, K. Liu, H. Li, Q. J. Wang, Y. Zhang, and H. Liang, "Flat-top pumped multi-millijoule mid-infrared parametric chirped-pulse amplifier at 10 kHz repetition rate," Laser Photonics Rev. **15**(6), 2000292 (2021).
2. U. Elu, T. Steinle, D. Sánchez, L. Maidment, K. Zawilski, P. Schunemann, U. Zeitner, C. Simon-Boisson, and J. Biegert, "Table-top high-energy 7 μm OPCPA and 260 mJ Ho:YLF pump laser," Opt. Lett. **44**(13), 3194–3197 (2019).
3. M. Kurucz, R. Flender, L. Haizer, R. S. Nagymihaly, W. Cho, K. T. Kim, S. Toth, E. Cormier, and B. Kiss, "2.3-cycle mid-infrared pulses from hybrid thin-plate post-compression at 7 W average power," Opt. Commun. **472**, 126035 (2020).

Optics EXPRESS

4. B.-H. Chen, E. Wittmann, Y. Morimoto, P. Baum, and E. Riedle, "Octave-spanning single-cycle middle-infrared generation through optical parametric amplification in $LiGaS_2$," Opt. Express **27**(15), 21306–21318 (2019).
5. L. Von Grafenstein, M. Bock, D. Ueberschaer, K. Zawilski, P. Schunemann, U. Griebner, and T. Elsaesser, "5 μm few-cycle pulses with multi-gigawatt peak power at a 1 kHz repetition rate," Opt. Lett. **42**(19), 3796–3799 (2017).
6. H. Liang, P. Krogen, Z. Wang, H. Park, T. Kroh, K. Zawilski, P. Schunemann, J. Moses, L. F. DiMauro, F. X. Kärtner, and K.-H. Hong, "High-energy mid-infrared sub-cycle pulse synthesis from a parametric amplifier," Nat. Commun. **8**(1), 141 (2017).
7. T. Feng, A. Heilmann, M. Bock, L. Ehrentraut, T. Witting, H. Yu, H. Stiel, S. Eisebitt, and M. Schnürer, "27 W 2.1 μm OPCPA system for coherent soft x-ray generation operating at 10 kHz," Opt. Express **28**(6), 8724–8733 (2020).
8. R. W. Boyd, *Nonlinear Optics* (Academic Press, 2019), 4th ed.
9. M. Kolesik and J. V. Moloney, "Modeling and simulation techniques in extreme nonlinear optics of gaseous and condensed media," Rep. Prog. Phys. **77**(1), 016401 (2013).
10. A. Couairon, L. Sudrie, M. Franco, B. Prade, and A. Mysyrowicz, "Filamentation and damage in fused silica induced by tightly focused femtosecond laser pulses," Phys. Rev. B **71**(12), 125435 (2005).
11. A. Dubietis, G. Tamošauskas, R. Šuminas, V. Jukna, and A. Couairon, "Ultrafast supercontinuum generation in bulk condensed media," Lith. J. Phys. **57**(3), 1 (2017).
12. T. Nagy, P. Simon, and L. Veisz, "High-energy few-cycle pulses: post-compression techniques," Adv. Phys.: X **6**, 1845795 (2021).
13. M. Sheik-Bahae, A. A. Said, and E. W. Van Stryland, "High-sensitivity, single-beam n_2 measurements," Opt. Lett. **14**(17), 955–957 (1989).
14. C. B. De Araújo, A. S. Gomes, and G. Boudebs, "Techniques for nonlinear optical characterization of materials: a review," Rep. Prog. Phys. **79**(3), 036401 (2016).
15. D. Milam and M. Weber, "Measurement of nonlinear refractive-index coefficients using time-resolved interferometry: application to optical materials for high-power neodymium lasers," J. Appl. Phys. **47**(6), 2497–2501 (1976).
16. M. Weber, D. Milam, and W. Smith, "Nonlinear refractive index of glasses and crystals," Opt. Eng. **17**(5), 175463 (1978).
17. M. Moran, C.-Y. She, and R. Carman, "Interferometric measurements of the nonlinear refractive-index coefficient relative to CS_2 in laser-system-related materials," IEEE J. Quantum Electron. **11**(6), 259–263 (1975).
18. K. Minoshima, M. Taiji, and T. Kobayashi, "Femtosecond time-resolved interferometry for the determination of complex nonlinear susceptibility," Opt. Lett. **16**(21), 1683–1685 (1991).
19. Á. Börzsönyi, Z. Heiner, A. Kovács, M. Kalashnikov, and K. Osvay, "Measurement of pressure dependent nonlinear refractive index of inert gases," Opt. Express **18**(25), 25847–25854 (2010).
20. I. Dancus, S. T. Popescu, and A. Petris, "Single shot interferometric method for measuring the nonlinear refractive index," Opt. Express **21**(25), 31303–31308 (2013).
21. P. Smith, W. Tomlinson, D. Eilenberger, and P. Maloney, "Measurement of electronic optical Kerr coefficients," Opt. Lett. **6**(12), 581–583 (1981).
22. R. Adair, L. Chase, and S. A. Payne, "Nonlinear refractive-index measurements of glasses using three-wave frequency mixing," J. Opt. Soc. Am. B **4**(6), 875–881 (1987).
23. R. Adair, L. Chase, and S. A. Payne, "Nonlinear refractive index of optical crystals," Phys. Rev. B **39**(5), 3337–3350 (1989).
24. B. Momgaudis, S. Guizard, A. Bilde, and A. Melninkaitis, "Nonlinear refractive index measurements using time-resolved digital holography," Opt. Lett. **43**(2), 304–307 (2018).
25. L. Lamaignère, G. Toci, B. Patrizi, M. Vannini, A. Pirri, S. Fanetti, R. Bini, G. Mennerat, A. Melninkaitis, L. Lukas, and J. Hein, "Determination of non-linear refractive index of laser crystals and ceramics via different optical techniques," Opt. Materials: X **8**, 100065 (2020).
26. I. Kang, T. Krauss, and F. Wise, "Sensitive measurement of nonlinear refraction and two-photon absorption by spectrally resolved two-beam coupling," Opt. Lett. **22**(14), 1077–1079 (1997).
27. A. Taylor, G. Rodriguez, and T. S. Clement, "Determination of n_2 by direct measurement of the optical phase," Opt. Lett. **21**(22), 1812–1814 (1996).
28. G. N. Patwardhan, J. S. Ginsberg, C. Y. Chen, M. M. Jadidi, and A. L. Gaeta, "Nonlinear refractive index of solids in mid-infrared," Opt. Lett. **46**(8), 1824–1827 (2021).
29. R. Šuminas, N. Garejev, A. Šuminienė, V. Jukna, G. Tamošauskas, and A. Dubietis, "Femtosecond filamentation, supercontinuum generation, and determination of n_2 in polycrystalline SBN," J. Opt. Soc. Am. B **37**(5), 1530–1534 (2020).
30. J. Pigeon, D. Matteo, S. Y. Tochitsky, I. Ben-Zvi, and C. Joshi, "Measurements of the nonlinear refractive index of $AgGaSe_2$, GaSe, and ZnSe at 10 μm," J. Opt. Soc. Am. B **37**(7), 2076–2079 (2020).
31. W. C. Hurlbut, Y.-S. Lee, K. Vodopyanov, P. Kuo, and M. Fejer, "Multiphoton absorption and nonlinear refraction of GaAs in the mid-infrared," Opt. Lett. **32**(6), 668–670 (2007).
32. A. D. Bristow, N. Rotenberg, and H. M. Van Driel, "Two-photon absorption and Kerr coefficients of silicon for 850–2200 nm," Appl. Phys. Lett. **90**(19), 191104 (2007).
33. W. Li, Y. Li, Y. Xu, J. Lu, P. Wang, J. Du, and Y. Leng, "Measurements of nonlinear refraction in the mid-infrared materials $ZnGeP_2$ and $AgGaS_2$," Appl. Phys. B **123**(3), 82 (2017).

Optics EXPRESS

34. B.-U. Sohn, C. Monmeyran, L. Kimerling, A. Agarwal, and D. Tan, "Kerr nonlinearity and multi-photon absorption in germanium at mid-infrared wavelengths," Appl. Phys. Lett. **111**(9), 091902 (2017).
35. M. Ferdinandus, J. Gengler, M. Tripepi, and C. Liebig, "Measurements of optical nonlinearities at mid-ir wavelengths using a modified z-scan technique," in *CLEO: Science and Innovations* (Optical Society of America, 2019), paper SF2G–4.
36. T. R. Ensley and N. K. Bambha, "Ultrafast nonlinear refraction measurements of infrared transmitting materials in the mid-wave infrared," Opt. Express **27**(26), 37940–37951 (2019).
37. K. Werner, M. G. Hastings, A. Schweinsberg, B. L. Wilmer, D. Austin, C. M. Wolfe, M. Kolesik, T. R. Ensley, L. Vanderhoef, A. Valenzuela, and E. Chowdhury, "Ultrafast mid-infrared high harmonic and supercontinuum generation with n_2 characterization in zinc selenide," Opt. Express **27**(3), 2867–2885 (2019).
38. Q. Li, R. Wang, F. Xu, X. Wang, Z. Yang, and X. Gai, "Third-order nonlinear optical properties of Ge–*As* – *Te*; chalcogenide glasses in mid-infrared," Opt. Mater. Express **10**(6), 1413–1420 (2020).
39. M. R. Ferdinandus, J. J. Gengler, K. L. Averett, K. T. Zawilski, P. G. Schunemann, and C. M. Liebig, "Nonlinear optical measurements of $CdSiP_2$ at near and mid-infrared wavelengths," Opt. Mater. Express **10**(9), 2066–2074 (2020).
40. R. DeSalvo, D. J. Hagan, M. Sheik-Bahae, G. Stegeman, E. W. Van Stryland, and H. Vanherzeele, "Self-focusing and self-defocusing by cascaded second-order effects in KTP," Opt. Lett. **17**(1), 28–30 (1992).
41. M. Takeda, H. Ina, and S. Kobayashi, "Fourier-transform method of fringe-pattern analysis for computer-based topography and interferometry," J. Opt. Soc. Am. **72**(1), 156–160 (1982).
42. S. Linden, H. Gießen, and J. Kuhl, "Xfrog-a new method for amplitude and phase characterization of weak ultrashort pulses," phys. stat. sol. (b) **206**(1), 119–124 (1998).
43. K. DeLong, R. Trebino, J. Hunter, and W. White, "Frequency-resolved optical gating with the use of second-harmonic generation," J. Opt. Soc. Am. B **11**(11), 2206–2215 (1994).
44. R. Trebino, K. W. DeLong, D. N. Fittinghoff, J. N. Sweetser, M. A. Krumbügel, B. A. Richman, and D. J. Kane, "Measuring ultrashort laser pulses in the time-frequency domain using frequency-resolved optical gating," Rev. Sci. Instrum. **68**(9), 3277–3295 (1997).
45. H. Li, C. Kam, Y. Lam, F. Zhou, and W. Ji, "Nonlinear refraction of undoped and Fe-doped $KTiOAsO_4$ crystals in the femtosecond regime," Appl. Phys. B **70**(3), 385–388 (2000).
46. H. Li, C. Kam, Y. Lam, and W. Ji, "Femtosecond z-scan measurements of nonlinear refraction in nonlinear optical crystals," Opt. Mater. **15**(4), 237–242 (2001).
47. M. Mero, L. Wang, W. Chen, N. Ye, G. Zhang, V. Petrov, and Z. Heiner, "Laser-induced damage of nonlinear crystals in ultrafast, high-repetition-rate, mid-infrared optical parametric amplifiers pumped at 1 μm," Proc. SPIE **11063**, 1106307 (2019).
48. M. Namboodiri, C. Luo, G. Indorf, T. Golz, I. Grguraš, J. H. Buss, M. Schulz, R. Riedel, M. J. Prandolini, and T. Laarmann, "Optical properties of Li-based nonlinear crystals for high power mid-IR OPCPA pumped at 1 μm under realistic operational conditions," Opt. Mater. Express **11**(2), 231–239 (2021).
49. M. Sheik-Bahae, D. C. Hutchings, D. J. Hagan, and E. W. Van Stryland, "Dispersion of bound electron nonlinear refraction in solids," IEEE J. Quantum Electron. **27**(6), 1296–1309 (1991).
50. D. Milam, "Review and assessment of measured values of the nonlinear refractive-index coefficient of fused silica," Appl. Opt. **37**(3), 546–550 (1998).
51. M. Baudrier-Raybaut, R. Haidar, P. Kupecek, P. Lemasson, and E. Rosencher, "Random quasi-phase-matching in bulk polycrystalline isotropic nonlinear materials," Nature **432**(7015), 374–376 (2004).
52. A. Marcinkevičiūtė, G. Tamošauskas, and A. Dubietis, "Supercontinuum generation in mixed thallous halides KRS−5 and KRS−6," Opt. Mater. **78**, 339–344 (2018).
53. P. S. Banks, M. D. Feit, and M. D. Perry, "High-intensity third-harmonic generation," J. Opt. Soc. Am. B **19**(1), 102–118 (2002).
54. V. G. Dmitriev, G. G. Gurzadyan, and D. N. Nikogosyan, *Handbook of Nonlinear Optical Crystals*, vol. 64 (Springer, 1999), 3rd ed.
55. D. Nikogosyan, *Nonlinear Optical Crystals: A Complete Survey* (Springer, 2005).
56. M. V. Pack, D. J. Armstrong, and A. V. Smith, "Measurement of the $\chi^{(2)}$ tensors of $KTiOPO_4$, $KTiOAsO_4$, $RbTiOPO_4$, and $RbTiOAsO_4$ crystals," Appl. Opt. **43**(16), 3319–3323 (2004).
57. V. Petrov, A. Yelisseyev, L. Isaenko, S. Lobanov, A. Titov, and J.-J. Zondy, "Second harmonic generation and optical parametric amplification in the mid-IR with orthorhombic biaxial crystals $LiGaS_2$ and LiGaSe2," Appl. Phys. B **78**(5), 543–546 (2004).
58. R. C. Miller, "Optical second harmonic generation in piezoelectric crystals," Appl. Phys. Lett. **5**(1), 17–19 (1964).
59. M. Sheik-Bahae, D. J. Hagan, and E. W. Van Stryland, "Dispersion and band-gap scaling of the electronic kerr effect in solids associated with two-photon absorption," Phys. Rev. Lett. **65**(1), 96–99 (1990).
60. R. DeSalvo, A. A. Said, D. J. Hagan, E. W. Van Stryland, and M. Sheik-Bahae, "Infrared to ultraviolet measurements of two-photon absorption and n_2 in wide bandgap solids," IEEE J. Quantum Electron. **32**(8), 1324–1333 (1996).